JOURNAL OF SPACECRAFT AND ROCKETS
Vol. 34, No. 3, May–June 1997

Cracking Characteristics of Dual-Wall Structures Following Simulated Orbital Debris Particle Impact

William P. Schonberg*
University of Alabama in Huntsville, Huntsville, Alabama 35899
and
Joel E. Williamsen†
NASA Marshall Space Flight Center, Huntsville, Alabama 35812

Data from 103 high-velocity impact tests of dual-wall structures are presented. From the test results, empirical models are developed for hole size and various cracking phenomena that accompany the perforation of a dual-wall spacecraft hull by an orbital debris particle. The models show that increasing the pressure wall thickness not only increases the ballistic limit of the dual-wall system but also reduces the cracking damage sustained by the system. In addition, for dual-wall systems with relatively thin pressure walls, placing a thermal insulation blanket at a position away from the pressure wall decreases the extent of the cracking damage sustained by the system. However, for dual-wall systems with relatively thick pressure walls, the extent of cracking damage sustained by the pressure wall is fairly independent of the location of the thermal insulation blanket.

Nomenclature

C_b	= bumper sound speed, $\sqrt{(E_b/\rho_b)}$, 5.04 km/s for aluminum
D_h	= pressure wall hole diameter, cm
d_{BL}	= ballistic limit diameter, a function of d_p, V_p, and θ_p, cm
d_p	= projectile diameter, cm
d_{pt}	= pressure wall petalling depth, cm
E_b	= bumper elastic modulus, 69 GPa for aluminum
L_{tt}	= maximum tip-to-tip crack length, cm
N	= number of data points
N_{cr}	= number of pressure wall cracks
R^2	= correlation coefficient
S	= stand-off distance between bumper and pressure wall, cm
S_2	= stand-off distance between thermal insulation blanket and pressure wall, cm
t_b	= bumper thickness, mm
t_w	= pressure wall thickness, mm
V_p	= projectile impact velocity, km/s
θ_p	= trajectory obliquity measured from outward-facing normal, deg or rad
ρ_b	= bumper material density, 2712 kg/m^3 for aluminum
σ	= max(σ_1, σ_2), GPa
σ_y	= pressure wall yield stress, 358 MPa for aluminum
σ_1, σ_2	= biaxial stresses in pressure wall due to internal module pressure, GPa

Introduction

ALL long-duration spacecraft in Earth orbit are subject to high-speed impacts by meteoroids and pieces of orbital debris. As a result, the threat of damage from such high-speed impacts has become a significant design consideration in the design of Earth-orbiting spacecraft. Habitable components of such spacecraft can be as long as 10 m and as large as 4.26 m in diameter and are typically pressurized at 1 atm. Historically, significant amounts of resources have been devoted to developing shielding for such structures as a means of reducing the penetration potential of high-speed on-orbit impacts.[1–5] Numerous studies have concluded that the level of protection afforded a spacecraft by a dual-wall structure significantly exceeds the level provided by an equal weight single wall of the same material. These studies have typically focused on simply whether or not the inner (or pressure) walls of candidate dual-wall structural systems would be perforated. However, the nature and extent of pressure wall damage in the event of a penetration have only recently begun to be explored.

In addition to a hole, the pressure wall of a dual-wall structure impacted by a high-speed particle can also experience cracking and petalling.[3,5,6] If module wall cracking were to occur on-orbit, unstable crack growth could develop and possibly lead to an unzipping of the module.[7] Thus, it is imperative to be able to characterize the cracking phenomena associated with the penetration of habitable dual-wall structures that are being developed for operation in the near-Earth orbital environment. Although pressure wall cracking and petalling has been observed in several previous laboratory studies of dual-wall structures under high-speed impact,[3,5,6] a systematic characterization of the various cracking phenomena has yet to be performed.

This paper presents the results of a study whose objective was to develop empirical models of hole size and of the various cracking phenomena that accompany the perforation of a dual-wall structural system. The cracking phenomena for which empirical equations were obtained in this study include effective pressure wall hole diameter, maximum tip-to-tip crack distance, depth of petal deformation, and number of cracks formed. The effects of pressure wall thickness, thermal insulation placement, and the effects of a biaxial stress field within the pressure wall (such as that which would exist in a pressurized habitable module) are included in the empirical models.

The significance of the work performed is that the model predictions can be fed directly into a survivability analysis for a habitable module built with such a wall system to determine whether or not module unzipping would occur under a specific set of impact conditions.[8,9] The likelihood of module unzipping over a structure's lifetime based on the environment to which it is exposed can also be determined in such an analysis. Furthermore, the prediction of hole size can be used as part of a survivability analysis to determine the time available for module evacuation prior to the onset of incapacitation due to air loss.

For the purposes of this study, effective hole diameter and crack length were defined as follows. The effective pressure wall hole diameter is taken to be that of a circle whose area equals the see-through area of the hole in the pressure wall. When there are two or more holes present, the definition of effective hole diameter is modified so that the effective hole diameter is that of a circle whose

Received May 15, 1996; revision received Jan. 29, 1997; accepted for publication Feb. 10, 1997.

*Professor, Civil and Environmental Engineering Department. Senior Member AIAA.

†Aerospace Engineer, Structural Development Branch, Mail Code ED-52. Member AIAA.

area equals the total see-through area of all of the holes present. In the event that a pressure wall hole is accompanied by large petals, the maximum tip-to-tip crack length is simply the largest distance between two crack tips in the star-shaped petal pattern. In those cases where petals and cracks were not formed, the hole in the pressure wall was typically an irregular shape with some discernible eccentricity. In such cases, the maximum tip-to-tip crack length is defined as the maximum width of the hole. Note that crack propagation effects for star-shaped patterns are undoubtedly determined by the interaction of the individual cracks. However, a single crack along the axial direction of a pressurized cylinder is more likely than a star-shaped crack path to produce unstable crack growth. Therefore, the approach taken in considering a single cracking parameter such as the maximum tip-to-tip crack length will result in conservative predictions of module unzipping.

Experimental Setup and Data

Figure 1 shows the impact of a dual-wall structure by a spherical projectile. To simulate the presence of thermal insulation in the spacecraft wall, a blanket of multilayer insulation (MLI) was inserted between the outer bumper and the pressure wall. In such a system, the bumper protects the pressure wall against perforation by causing the disintegration of the impacting projectile and the creation of a debris cloud, which imparts a significantly lower impulse per unit area to the pressure wall. The pressure wall area over which the impulsive load is distributed is governed by the extent to which the projectile and bumper material fragment, melt, or vaporize; by the location of the MLI within the dual-wall system; and by the spacing between the bumper and the pressure wall.

The results from 103 high-speed impact tests were used to develop the empirical equations for the various pressure wall damage characteristics considered. The impact conditions were chosen to simulate orbital debris impact of lightweight space structures as closely as possible and still remain within the realm of experimental feasibility. Kessler et al.[10] state that the average density for orbital debris particles is approximately 2.8 g/cm^3, which is similar to that of aluminum. Therefore, aluminum 1100-0 was used as the projectile material in all of the tests.

The projectiles were fired using a two-stage light gas gun at the NASA Marshall Space Flight Center. Projectile integrity was verified by inspection of high-speed camera photographs of the projectile just before impact. The accuracy of the impact velocity was ± 0.1 km/s whereas that of the impact angle was ± 1 deg. Tip-to-tip crack lengths were measured with a standard ruler, whereas equivalent single-hole diameters were obtained from calculated through-hole areas. These areas were determined from a projection of the pressure wall hole outline on a sheet of graph paper. It is estimated that the longer crack length measurements (i.e., crack lengths in excess of 10 cm) were accurate to ± 0.5 cm whereas the shorter crack length measurements (i.e., crack lengths shorter than 5 cm) were accurate to ± 0.1 cm.

Although orbital debris particles may take on any shape, the tests were performed using spherical projectiles to ensure repeatability and consistency. In all of the tests, the bumper material was 6061-T6 aluminum whereas that of the pressure wall was aluminum 2219-T87. To assess the effect of the internal spacecraft pressure on pressure wall damage, two pressure wall stress states were considered: unstressed and biaxially stressed. The biaxial stress field was induced in the pressure walls of some test specimens by applying distributed tensile loads to the pressure wall plates. Table 1 contains a summary of the test parameters considered in this study.

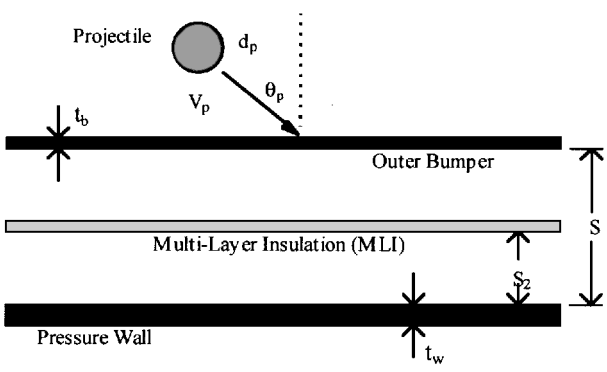

Fig. 1 Hypervelocity impact of a generic dual-wall structure.

Table 1 Experimental test parameters

Parameter	Unstressed		Stressed
	$t_w = 3.2$ mm	$t_w = 4.8$ mm	$t_w = 3.2$ mm only
d_p, cm	0.64–1.27	0.80–1.59	0.64–0.95
θ_p, deg	0, 45, 65	0, 45, 65	0, 45
V_p, km/s	4.05–7.22	6.21–6.88	4.14–7.21
t_b, mm	1.0–1.6	1.27	1.6
S, cm	10.16, 11.43	10.16, 11.43	10.16
S_2/S	0.0, 0.5	0.0, 0.5	0.0
σ_1, σ_2, MPa	n/a	n/a	68, 34 124, 62

The magnitudes of the induced stress fields were similar to the stress levels expected in the walls of a cylindrical module with a 4.26-m inner diameter pressurized at 1 atm. The biaxial stress states were induced in the pressure walls of the stressed systems by applying distributed tensile loads to the pressure wall plates. Triaxial 0/45/90 deg rosette strain gauges were applied to each pressure wall to monitor the stress state in the wall while the tensile loads were applied. These loads were applied to the pressure walls using power screws that were tightened incrementally and in a specific sequence, thereby avoiding local yielding of the pressure wall and the screws. Additional information regarding the test fixture and load application can be found in Ref. 11.

Empirical Predictor Equations

Tables 2–4 contain the actual test data used subsequently to develop the empirical predictor equations. Tables 2 and 3 contain the data for dual-wall systems with unstressed 3.2- and 4.8-mm pressure walls, respectively, whereas Table 4 contains the data for dual-wall systems with stressed pressure walls. Based on the test data in Tables 2–4, three sets of empirical equations were developed; each set contains an equation for equivalent pressure wall hole diameter, maximum tip-to-tip crack length, number of cracks created, and depth of pressure wall deformation. The first and second set are applicable to dual-wall systems with 3.2- and 4.8-mm unstressed pressure walls, respectively, whereas the third is applicable to such systems with 3.2-mm stressed pressure walls. Inspection of Table 1 reveals additional limitations in the applicability of the equations in each set. Of note is that whereas the tests using unstressed 3.2-mm pressure walls were performed over some range of impact velocities and bumper thicknesses, the tests using unstressed 4.8-mm pressure walls were all performed using a single bumper thickness and over a very small range of impact velocities. Hence, the equations for the dual-wall systems with unstressed 3.2-mm pressure walls contain bumper thickness and impact velocity dependencies whereas those for the dual-wall systems with unstressed 4.8-mm pressure walls do not.

The empirical predictor equations developed for the various phenomena under consideration were all of the form

$$X = A(1 - S_2/S)^B f(\theta_p)\{1 - \exp[-D(d_p/d_{\mathrm{BL}} - 1)]\} \times (V_P/C_b)^E (t_b/d_{\mathrm{BL}})^F (\sigma/\sigma_y)^G \quad (1)$$

where X is the measure of the particular phenomenon under consideration (e.g., hole diameter, number of cracks, etc.). Ballistic limit diameters for the various systems considered in this study were obtained using the equations given in Ref. 12. Because the presence of a biaxial stress field identical to the one considered in this study was previously shown not to significantly affect the ballistic limit of the dual-wall systems under consideration,[13] the equations in Ref. 12 were used for the stressed as well as for the unstressed systems. In Eq. (1), the function $f(\theta_p) = \cos C\theta_p$ was used except for the case of unstressed 3.2-mm pressure walls, where $f(\theta_p) = e^{-C\theta_p}$ (θ_p in radians). This alternative form was used because measured quantities were observed to decrease rapidly with increasing obliquity for 3.2-mm pressure walls.

Table 2 Impact test parameters and data, unstressed dual-wall systems with t_w = 3.2 mm

Test no.	t_b, mm	S_2, cm	S, cm	V_p, km/s	θ_p, deg	d_p, cm	D_h, cm	L_{tt}, cm	N_{cr}	d_{pt}, cm
MLI on pressure wall										
002B	1.6	0	10.16	6.51	45	0.80	——	4.24	3	——
003A	1.0	0	10.16	6.51	45	0.80	3.43	11.99	5	1.27
201A	1.6	0	10.16	4.33	45	0.64	0.84	——	——	——
201B	1.0	0	10.16	5.51	45	0.64	1.17	——	——	——
203G	1.0	0	10.16	4.07	65	0.89	0.38	——	1	——
205B	1.6	0	10.16	4.62	45	0.89	0.43	——	1	——
205C	1.6	0	10.16	5.30	45	0.64	0.97	——	1	——
207A	1.6	0	10.16	5.86	65	0.76	——	0.38	——	——
207B	1.6	0	10.16	6.47	65	0.76	0.36	—-	1	——
210B	1.6	0	10.16	5.67	65	0.89	0.33	——	1	——
210D	1.6	0	10.16	7.05	65	0.89	0.81	——	1	——
211B	1.6	0	10.16	5.88	45	0.89	2.13	——	——	——
211D	1.6	0	10.16	6.84	45	0.89	2.79	5.61	4	1.27
212B	1.6	0	10.16	6.38	45	0.76	1.57	——	——	——
324	1.0	0	10.16	4.05	45	0.80	1.80	3.00	——	——
325	1.6	0	10.16	4.14	45	0.80	1.12	2.97	2	——
335	1.0	0	10.16	4.07	45	0.64	0.97	——	——	——
336	1.0	0	10.16	4.47	45	0.64	0.99	3.33	4	0.76
337	1.0	0	10.16	6.90	45	0.80	2.13	8.92	4	1.27
338	1.0	0	10.16	6.98	45	0.80	2.44	9.30	5	1.60
339	1.0	0	10.16	6.49	45	0.95	4.37	22.30	5	1.27
P21D	1.6	0	10.16	5.85	0	0.76	2.62	——	——	——
P33B	1.0	0	10.16	4.85	0	0.64	2.11	——	1	——
T2-15	1.0	0	10.16	4.98	0	0.95	8.74	15.34	6	5.08
T2-17	1.6	0	10.16	4.62	0	0.95	8.31	16.66	6	6.35
EH2A	1.6	0	10.16	6.99	0	0.80	3.58	26.57	4	2.54
EH2C	1.6	0	10.16	6.58	0	0.80	——	22.66	3	2.54
EH2D	1.6	0	10.16	6.62	0	0.80	3.23	23.04	3	1.91
EH2E	1.6	0	10.16	6.70	0	0.80	6.88	17.93	6	3.81
EH4A	1.6	0	10.16	6.13	0	0.80	2.21	12.70	4	3.81
EH4B	1.6	0	10.16	6.70	0	0.80	4.06	10.16	5	3.81
EH-M4	1.6	0	10.16	6.92	0	0.80	2.03	15.95	4	2.54
PREH1	1.6	0	10.16	6.99	0	0.80	2.79	18.29	4	1.91
PREH2	1.6	0	10.16	6.88	0	0.80	5.05	20.24	5	1.91
3011A	1.0	0	10.16	7.02	0	0.80	6.55	18.72	6	5.08
3011B	1.0	0	10.16	6.75	0	0.80	5.08	20.32	6	5.08
3020A	1.6	0	10.16	6.65	0	0.80	2.62	22.28	4	3.18
3020B	1.6	0	10.16	7.05	0	0.80	2.36	25.70	——	2.54
3024B	1.6	0	10.16	7.02	0	0.80	——	17.37	——	1.60
3028A	1.6	0	10.16	7.01	45	0.80	1.40	3.68	2	0.64
3227A	1.6	0	10.16	6.80	0	0.95	9.27	30.73	6	7.62
3227B	1.6	0	10.16	6.70	0	0.95	9.50	19.86	4	7.62
MLI not on pressure wall										
1690	1.27	5.72	11.43	6.50	0	0.80	——	10.16	2	——
1698	1.27	5.72	11.43	6.61	0	0.95	6.58	18.29	7	4.83
1709	1.27	5.72	11.43	6.42	45	0.80	1.85	2.54	1	——
1726	1.27	5.72	11.43	6.58	45	0.95	2.87	4.06	——	——
1753	1.27	5.72	11.43	6.62	65	0.95	0.99	1.27	1	——
1764	1.27	5.72	11.43	6.34	0	1.11	10.41	18.80	4	8.38
1766	1.27	5.72	11.43	6.33	45	1.11	3.10	4.17	——	——
1767	1.27	5.72	11.43	6.53	65	1.11	1.30	1.80	1	——
1768	1.27	5.72	11.43	6.10	65	1.27	2.59	2.95	——	——
3401A	1.6	5.08	10.16	7.22	0	0.80	2.01	9.07	5	1.60
3401B	1.6	5.08	10.16	7.09	0	0.80	——	8.92	5	1.60
3401C	1.6	5.08	10.16	6.12	0	0.80	——	8.61	4	——
3401D	1.6	5.08	10.16	5.25	0	0.80	——	6.15	4	——
3402A	1.6	5.08	10.16	7.18	0	0.80	——	7.72	4	1.27
3402B	1.6	5.08	10.16	7.10	0	0.80	——	5.51	5	1.27
3402C	1.6	5.08	10.16	6.17	0	0.80	——	7.26	4	——
3402D	1.6	5.08	10.16	5.02	0	0.80	——	——	4	——
3404A	1.6	5.08	10.16	6.85	0	0.95	8.05	24.38	5	5.08
3404B	1.6	5.08	10.16	6.85	0	0.95	6.76	15.24	7	5.08
3404C	1.6	5.08	10.16	6.23	0	0.95	4.75	17.68	6	4.45
3404D	1.6	5.08	10.16	5.50	0	0.95	4.57	13.23	7	4.45

The functional dependence of Eq. (1) on projectile diameter was chosen for the following two reasons. First, as it should be, the quantity X is zero when the projectile diameter equals the ballistic limit diameter of the particular system under consideration. Second, the form of Eq. (1) adequately represents the general type of phenomenology expected for damage growth as projectile diameter is increased beyond the ballistic limit.[14] The values of the constants $A-G$ were obtained using a simplex curve fitting algorithm.

Table 5 presents the values of these constants and appropriate correlation coefficients for the various equations developed; the final columns in these tables show the number of data points used to obtain a particular equation. The 0 values in Table 5 indicate a parameter that was not included in the regression model either due to the nature of the tests performed (e.g., unstressed in Tables 2 and 3) or the nature of the experimental data obtained (e.g., only one bumper thickness or MLI position). As can be seen from the correlation

Table 3 Impact test parameters and data, unstressed dual-wall systems with t_w = 4.8 mm

Test no.	t_b, mm	S_2, cm	S, cm	V_p, km/s	θ_p, deg	d_p, cm	D_h, cm	L_{tt}, cm	N_{cr}	d_{pt}, cm
218B	1.0	0	10.16	6.40	45	0.89	1.78	1.78	1	——
218C	1.0	0	10.16	6.88	45	0.89	1.85	3.10	1	0.25
1712	1.27	0	11.43	6.56	45	0.80	1.93	2.54	1	——
1735	1.27	0	11.43	6.60	45	0.95	2.69	3.81	1	0.25
1756	1.27	0	11.43	6.65	65	0.95	1.22	1.32	1	0.25
1759	1.27	0	11.43	6.21	0	1.11	4.09	4.62	1	——
1772	1.27	0	11.43	6.57	45	1.11	3.33	4.14	1	0.25
1773	1.27	0	11.43	6.57	65	1.11	0.58	0.64	1	0.25
1774	1.27	0	11.43	6.21	65	1.27	0.71	1.60	1	0.25
1825	1.27	0	11.43	6.39	0	0.95	3.58	4.14	1	——
HS-10	1.27	5.72	11.43	6.40	0	0.80	0.23	1.65	3	——
HS-11	1.27	5.72	11.43	6.41	0	0.95	3.25	5.66	3	1.27
HS-12	1.27	5.72	11.43	6.32	0	1.11	5.11	5.99	1	1.60
HS-13	1.27	5.72	11.43	6.40	45	0.80	0.91	1.37	1	——
HS-14	1.27	5.72	11.43	6.35	45	0.95	2.39	3.18	1	——
HS-15	1.27	5.72	11.43	6.40	45	1.11	2.74	3.63	1	——
HS-17	1.27	5.72	11.43	6.47	65	0.95	0.58	0.71	1	0.25
HS-18	1.27	5.72	11.43	6.46	65	1.11	2.26	2.90	1	0.25
UAH-1	1.6	5.72	11.43	6.70	0	1.27	5.84	15.24	7	3.81
UAH-3	1.6	5.72	11.43	6.42	0	1.59	6.10	8.64	2	——
UAH-6	1.6	5.72	11.43	6.50	0	1.59	6.35	14.22	3	——
WS-76	1.27	8.89	11.43	6.63	0	1.27	4.90	5.33	1	0.25
WS-34	1.27	8.89	11.43	6.72	0	0.95	2.06	2.54	1	1.78

Table 4 Impact parameters and test data, stressed dual-wall systems with t_w = 3.2 mm

Test no.	t_b, mm	S_2, cm	S, cm	V_p, km/s	θ_p, deg	d_p, cm	σ, MPa	D_h, cm	L_{tt}, cm	N_{cr}	d_{pt}, cm
FP-01	1.6	0	10.16	6.88	0	0.95	68	10.46	38.96	6	8.89
FP-04	1.6	0	10.16	6.87	0	0.95	34	10.06	28.96	7	7.62
FP-05	1.6	2.29	10.16	6.83	0	0.95	124	8.81	22.71	7	7.62
FP-06	1.6	2.29	10.16	6.99	0	0.95	124	8.81	31.09	5	7.62
FP-07	1.6	2.29	10.16	6.84	0	0.95	124	8.66	28.22	5	7.62
FP-13	1.6	0	10.16	4.14	0	0.64	68	0.76	1.02	1	0.25
FP-16	1.6	0	10.16	2.60	0	0.64	68	1.12	1.27	1	1.27
FP-18	1.6	0	10.16	5.32	45	0.64	68	0.36	0.76	1	0.25
FP-19	1.6	0	10.16	6.50	45	0.64	68	0.43	1.02	1	0.25
FP-20	1.6	0	10.16	7.05	45	0.64	68	0.46	0.51	1	0.25
FP-21	1.6	0	10.16	5.19	0	0.80	68	3.89	9.75	5	3.81
FP-22	1.6	0	10.16	5.98	0	0.80	68	4.11	9.09	4	5.08
FP-23	1.6	0	10.16	7.21	0	0.80	68	2.84	22.99	4	6.35
FP-24	1.6	0	10.16	6.90	45	0.80	68	1.80	2.54	1	0.25
FP-25	1.6	0	10.16	7.29	45	0.80	68	1.02	8.03	3	1.27
WG-02	1.6	2.29	10.16	6.86	0	0.95	68	10.29	28.45	6	8.89
WG-03	1.6	2.29	10.16	6.88	0	0.95	124	10.31	31.60	7	7.62

coefficients in Table 5, the empirical equations developed have a rather good fit to the experimental data.

Note that although constants $B-G$ are dimensionless, constant A is not. In fact, it is the units of constant A that dictate the units of the particular quantity under consideration. Figures 2–4 compare regression equation predictions and experimental data for dual-wall systems with 3.2-mm-thick pressure walls that are impacted at velocities of ±6.5 km/s. These plots, which are representative of the other comparison plots not shown, indicate a rather good fit of the regression predictions to the experimental data.

Comments and Observations

The effects of pressure wall thickness, MLI placement, and the presence of a pressure wall biaxial stress field on the cracking response of a pressure wall in an aluminum dual-wall system under high-speed projectile impact were studied by applying the equations developed to the impact of a variety of aluminum dual-wall systems. To be able to use the equations generated for a dual-wall system with an unstressed 4.8-mm pressure wall, results were generated for spherical projectiles normally impacting dual-wall systems at a nominal velocity of 6.5 km/s.

For systems with unstressed pressure walls, the bumper was 1.27 mm thick and 11.43 cm away from the pressure wall; two MLI positions were considered (against the pressure wall and midway between the bumper and the pressure wall), as were two pressure wall thicknesses (3.2 and 4.8 mm). For systems with stressed pressure walls, the bumper was 1.6 mm thick and was 10.16 cm away from the pressure wall. In these systems, the MLI was placed against the wall and only one pressure wall thickness was considered (3.2 mm) due to the nature of the data used to derive the equations for such systems; the value of σ corresponding to a wall thickness of 3.2 mm was calculated to be 68 MPa. To allow comparison of the results obtained for systems with stressed pressure walls, results were also generated for geometrically identical dual-wall systems with unstressed pressure walls and with the MLI directly against the pressure wall.

The comparisons presented herein are based on data obtained from impact tests whose upper limit on impact velocity was approximately 7 km/s. Because orbital debris particles can impact spacecraft at speeds up to 16 km/s, the equations developed apply to only a portion of the debris threat. Therefore, to be able to perform a complete survivability analysis, the equations must be extended to cover the entire impact velocity regime. Because extensive test data are not available beyond 7 km/s, it is anticipated that the extension to higher velocities will have to be done using information provided by hydrocodes and materials scaling.

Table 5 Regression constants

	A, cm[a]	B	C	D	E	F	G	R^2	N
				Unstressed, $t_w = 3.2$ mm					
D_h	2.357	0.112	1.436	0.521	1.456	−1.458	0	0.89	51
L_{tt}	24.221	0.727	1.632	0.513	3.475	−0.429	0	0.87	49
N_{cr}	3.223	0.135	0.765	1.833	0.208	−0.723	0	0.81	51
d_{pt}	5.324	0.183	2.265	0.426	1.106	−0.914	0	0.88	35
				Unstressed, $t_w = 4.8$ mm					
D_h	7.013	0.0297	1.871	2.597	0	0	0	0.96	23
L_{tt}	14.364	0.0625	2.538	1.732	0	0	0	0.84	23
N_{cr}	3.541	−0.0473	2.483	4.014	0	0	0	0.65	23
d_{pt}	13.001	−0.843	5.914	0.262	0	0	0	0.95	13
				Stressed, $t_w = 3.2$ mm					
D_h	5.425	0	4.549	0.432	5.961	0	−0.161	0.95	17
L_{tt}	30.632	0	5.466	0.259	6.133	0	−0.0706	0.97	17
N_{cr}	2.967	0	3.344	2.951	2.406	0	−0.129	0.94	17
d_{pt}	5.561	0	6.749	1.027	3.664	0	−0.0609	0.99	17

[a]Except for N_{cr}, which is dimensionless.

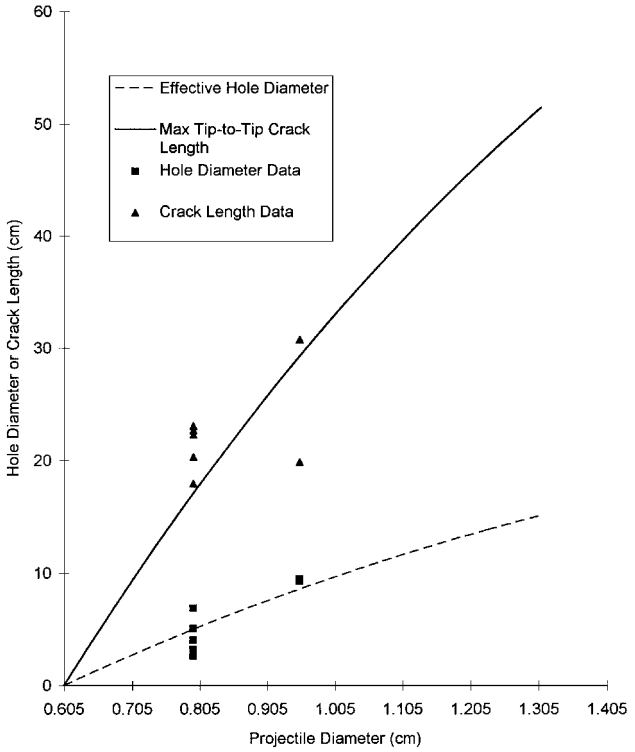

Fig. 2 Comparison of prediction and experiment: normal impact, MLI on pressure wall, 1.27-mm bumper, and 3.2-mm pressure wall.

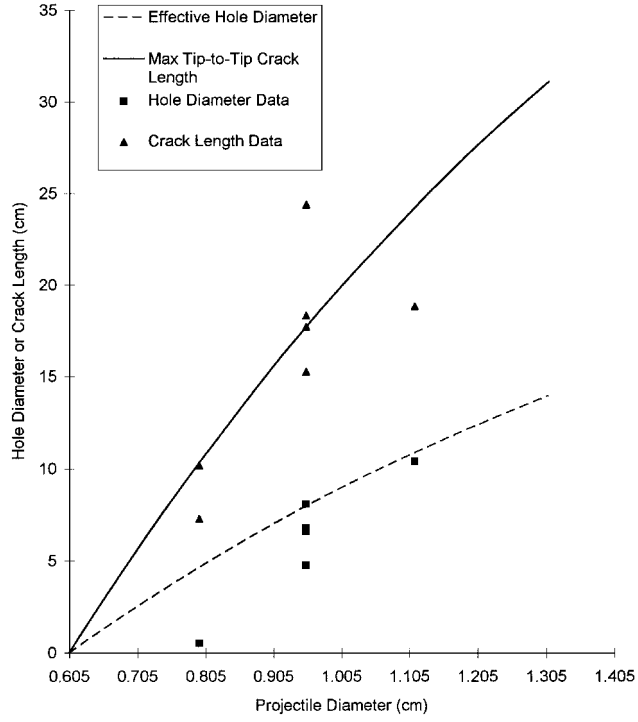

Fig. 3 Comparison of prediction and experiment: normal impact, MLI at center, 1.27-mm bumper, and 3.2-mm pressure wall.

Effect of Pressure Wall Thickness

Table 6 shows the ratios of hole diameter, etc., in dual-wall systems with 3.2-mm pressure walls to corresponding values in dual-wall systems with 4.8-mm pressure walls for the two different MLI locations considered and for three different projectile diameters. The projectile diameters considered were chosen to show the effect of steadily increasing the projectile diameter beyond the ballistic limit value for the system with a 1.27-mm bumper and a 4.8-mm pressure wall (denoted by $d_{BL}^{4.8}$). As can be seen in Table 6, the response ratios are all greater than 2.0, regardless of MLI position. Thus, it is quite apparent that increasing the thickness of the pressure wall from 3.2 to 4.8 mm significantly reduces the damage sustained by the pressure wall, especially for very large projectile diameters.

Closer examination of Table 6 reveals that the response ratios for $S_2/S = 0.5$ are generally less than corresponding response ratios when $S_2/S = 0.0$. Apparently, the extent of cracking damage decreased in dual-wall systems with 3.2-mm pressure walls when the MLI was moved away from the pressure wall, whereas the extent of damage in corresponding systems with 4.8 mm pressure walls remained essentially constant. The reasons for this behavior are discussed in the next section.

Effect of MLI Placement

Table 7 shows the ratios of hole diameter, etc., in dual-wall systems with $S_2/S = 0.0$ to corresponding values in dual-wall systems with $S_2/S = 0.5$; no projectile diameters are specified because the terms involving projectile diameter cancel in making the ratios for a dual-wall system with a given pressure wall thickness. As is evident in Table 7, moving the MLI away from a thin pressure wall (i.e., 3.2 mm thick) to a position midway in between the bumper and pressure wall significantly reduced the extent of pressure wall cracking damage. Crack lengths for systems with the MLI on a thin pressure wall exceeded those in systems with the MLI at the center of the dual-wall system by nearly 66%. This result reinforces the conclusions reached in two previous studies of the effect of MLI placement on the high-speed impact response of dual-wall systems with thin pressure walls.[15,16] In addition, effective hole diameters and depths of petal deformations were also larger when the MLI was placed directly against a thin pressure wall than in corresponding systems where the MLI was removed from the pressure wall, but only by approximately 10%.

Of further interest in Table 7 is that the effect of MLI location just described for dual-wall systems with a 3.2-mm pressure wall were not present in dual-wall systems with a 4.8-mm pressure wall.

Table 6 Effect of pressure wall thickness: ratio of 3.2-mm pressure wall response to 4.8-mm pressure wall response

Response characteristic	Projectile diameter $d_p = 1.5\,d_{\mathrm{BL}}^{4.8}$	$d_p = 2.0\,d_{\mathrm{BL}}^{4.8}$	$d_p \gg d_{\mathrm{BL}}^{4.8}$
	Unstressed systems, $S_2/S = 0.0$		
D_h	2.613	2.949	4.375
L_{tt}	5.474	5.526	7.972
N_{cr}	2.719	2.843	2.965
d_{pt}	6.360	4.936	2.258
	Unstressed systems, $S_2/S = 0.5$		
D_h	2.468	2.785	4.472
L_{tt}	3.453	3.487	5.029
N_{cr}	2.352	2.459	2.565
d_{pt}	3.123	2.424	1.109

Table 7 Effect of MLI placement: ratio of pressure wall response for $S_2/S = 0$ to response for $S_2/S = 0.5$ (unstressed systems)

Characteristic	$t_w = 3.2$ mm	$t_w = 4.8$ mm
D_h	1.081	1.021
L_{tt}	1.655	1.044
N_{cr}	1.098	0.950
d_{pt}	1.135	0.557

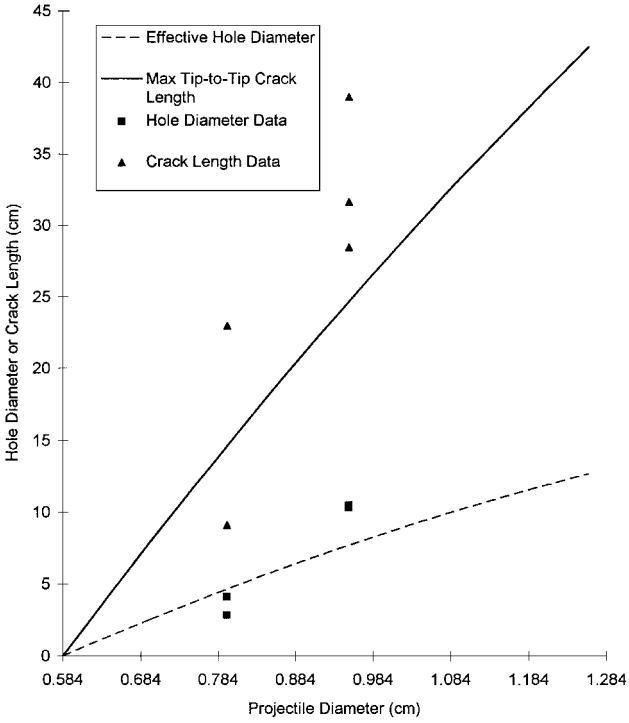

Fig. 4 Comparison of prediction and experiment: normal impact, 1.6-mm bumper, and stressed 3.2-mm pressure wall.

Thus, although there are significant benefits to be gained in moving the MLI to the center of a dual-wall system with a relatively thin pressure wall, these benefits are negligible in a dual-wall system with a relatively thick pressure wall. Moving the MLI away from a pressure wall results in a time lag between the impact on the pressure wall of the debris cloud containing fragmented and/or molten projectile and bumper material and the later-time slap of the MLI blanket on the pressure wall. This time lag in turn results in a lower impulsive load per unit time, which, in the case of the relatively thin 3.2-mm pressure walls, reduces the crack lengths produced by the impact. However, the removal of the MLI from the pressure wall has only a minimal effect on the 4.8-mm pressure wall. In such a case, the wall stiffness is sufficiently high so as to allow only small deformations, even when the MLI is against the pressure wall and the impulsive load per unit time is at its largest value.

Table 8 Effect of biaxial stress field: ratio of 3.2-mm unstressed pressure wall response to 3.2-mm stressed pressure wall response; MLI against pressure wall

Response characteristic	Projectile diameter $d_p = 1.5\,d_{\mathrm{BL}}^{3.2}$	$d_p = 2.0\,d_{\mathrm{BL}}^{3.2}$	$d_p \gg d_{\mathrm{BL}}^{3.2}$
D_h	1.038	0.902	0.316
L_{tt}	1.160	0.878	0.200
N_{cr}	1.136	1.392	1.318
d_{pt}	0.831	0.980	0.628

Effect of Biaxial Stress Field

The study of the effects of a biaxial stress field on pressure wall cracking phenomena yielded some interesting results and a few surprises. In a manner analogous to Table 6, Table 8 shows the ratio of hole diameter, etc., for dual-wall systems with unstressed pressure walls to that in dual-wall systems with stressed pressure walls for three different projectile diameters. However, in Table 8 the projectile diameters are related to the ballistic limit of a dual-wall system with a 1.27-mm bumper and a 3.2-mm pressure wall (denoted by $d_{\mathrm{BL}}^{3.2}$).

According to Table 8, for projectile diameters that are moderately in excess of the ballistic limit diameter, the effect of the biaxial stress field is minimal, that is, all response ratios are close to unity. However, when the projectile diameter is large, the effects of the stress field become very pronounced: hole diameters, crack lengths, and petal deformation depths in the stressed pressure walls exceed those in unstressed pressure walls by factors of approximately 3, 5, and 1.5, respectively.

Apparently, for dual-wall systems with thin pressure walls that are impacted by particles considerably above the ballistic limit, the presence of the biaxial stress field caused larger holes and fewer, but longer, cracks with more bulging than in corresponding unstressed pressure wall plates of dual-wall systems impacted by similar particles. Such behavior is expected because the presence of the stress field in the pressure wall results in preferred cracking directions. Rather than develop in an arbitrary fashion, cracks are created along directions that are perpendicular to the direction of the maximum stress component. Because there are fewer cracks, the surface energy that existed in an unstressed pressure wall with many cracks is used instead to elongate the cracks. These results agree generally with results in Ref. 13.

Conclusions

Based on the results obtained, several important conclusions that affect the design of perforation resistant Earth-orbiting dual-wall structures can be made. First, increasing the thickness of the pressure wall from 3.2 to 4.8 mm not only increases the ballistic limit of the dual-wall system, but also reduces the cracking damage sustained by the system. Second, for 3.2-mm (i.e., relatively thin) pressure walls, moving the MLI off the pressure wall has the effect of decreasing the extent of the cracking damage sustained by the pressure wall in a dual-wall system. This effect is especially significant for the maximum tip-to-tip crack length sustained by the pressure wall during perforation. Third, for 4.8-mm (i.e., relatively thick) pressure walls, moving the MLI off the pressure wall has a negligible effect on hole diameter and crack length. Finally, for a dual-wall system with a 3.2-mm pressure wall, the presence of a biaxial stress field can have a significant effect on pressure wall response, but only for very large projectile diameters (i.e., greater than at least twice the ballistic limit diameter). For projectile diameters just above the ballistic limit diameter, the effect of a biaxial stress field is minimal.

Acknowledgments

The authors are grateful for the support provided by the NASA/American Society for Engineering Education Summer Faculty Fellowship Program and the NASA Marshall Space Flight Center Structural Development Branch. The authors would also like to acknowledge the work of A. Nolen, M. McCain, and M. Hovater (NASA Marshall Space Flight Center), M. Rucker (NASA White Sands Test Facility), and R. Hayami (University of Alabama in

Huntsville Aerophysics Research Center) in performing the high-speed impact tests that made this study possible.

References

[1]Maiden, C. J., Gehring, J. W., and McMillan, A. R., "Investigation of Fundamental Mechanism of Damage to Thin Targets by Hypervelocity Projectiles," General Motors Defense Research Lab., TR-63-225, Santa Barbara, CA, Sept. 1963.

[2]McMillan, A. R., "Experimental Investigation of Simulated Meteoroid Damage to Various Spacecraft Structures," NASA CR-915, Jan. 1965.

[3]Burch, G. T., "Multi-plate Damage Study," U.S. Air Force Armament Lab., AFATL-TR-67-116, Eglin AFB, FL, Sept. 1967.

[4]Lundeberg, J. F., Stern, P. H., and Bristow, J. R., "Meteoroid Protection for Spacecraft Structures," NASA TM-54201, Oct. 1965.

[5]Schonberg, W. P., Bean, A. J., and Darzi, K., "Hypervelocity Impact Physics," NASA CR-4343, Jan. 1991.

[6]Schonberg, W. P., "Aluminum 2219-T87 vs. 5456-H116: A Comparative Study of Pressure Wall Materials in Dual-Wall Structures Under Hypervelocity Impact," *Acta Astronautica*, Vol. 26, No. 11, 1992, pp. 799–812.

[7]"Common Module Shell Unzipping Due to Meteoroid/Orbital Debris Strikes," Space Station Freedom Program Office, GSS-40.05-RPT-6-001, Reston, VA, March 1994.

[8]Williamsen, J. E., "Vulnerability of Manned Spacecraft to Crew Loss from Orbital Debris Penetration," NASA TM-108452, April 1994.

[9]"Micrometeoroid and Orbital Debris Induced Catastrophic Failure Prediction Methods," Space Station Freedom Program Office, GSS-40.05-RPT-6-003, Reston, VA, April 1994.

[10]Kessler, D. J., Reynolds, R. C., and Anz-Meador, P. D., "Orbital Debris Environment for Spacecraft Designed to Operate in Low Earth Orbit," NASA TM-100471, April 1989.

[11]Williams, D. R., "Biaxially Stressed Hypervelocity Impact Tests for Space Station Common Module Structural Member Selection," Boeing Aerospace Corp., D683-10538-1, Huntsville, AL, Jan. 1992.

[12]Christiansen, E. L., "Design and Performance Equations for Advanced Meteoroid and Debris Shields," *International Journal of Impact Engineering*, Vol. 14, Nos. 1–4, 1993, pp. 145–156.

[13]Schonberg, W. P., "Effect of Internal Stress Fields on the Perforation Response of Dual-Wall Structures Under Hypervelocity Impact," *International Journal of Impact Engineering*, Vol. 14, Nos. 1–4, 1993, pp. 637–646.

[14]Schonberg, W. P., and Williamsen, J. E., "Cracking Characteristics of Multi-Wall Pressure Vessels Following Hypervelocity Projectile Impact," *Proceedings of the 1996 ASME PVP Conference on Structures Under Extreme Loading Conditions*, edited by Y. S. Shin and J. A. Zukas, ASME PVP-Vol. 235, American Society of Mechanical Engineers, New York, 1996, pp. 137–148.

[15]Jolly, W. H., and Williamsen, J. E., "Ballistic Limit Curve Regression for Freedom Station Orbital Debris Shielding," AIAA Paper 92-1463, March 1992.

[16]Schonberg, W. P., "Effect of Multi-Layer Thermal Insulation Thickness and Location on the Hypervelocity Impact Response of Dual-Wall Structures," *Acta Astronautica*, Vol. 32, No. 9, 1994, pp. 577–589.

F. S. Milos
Associate Editor